Available online at www.sciencedirect.com

SciVerse ScienceDirect

Ceramics International 39 (2013) 7583–7587

CERAMICS INTERNATIONAL

www.elsevier.com/locate/ceramint

Effects of a non-magnetic CuZn ferrite layer on cofiring and electrical properties of a low-fire, multilayer NiCuZn ferrite inductor

Yi-Ling Tung[a], Jau-Ho Jean[a,*], Ya-Hwang Cheng[b]

[a]*Department of Materials Science and Engineering, National Tsing HuaUniversity, Hsinchu, Taiwan*
[b]*Advanced Ceramic X Corp., Hsinchu, Taiwan*

Received 18 February 2013; accepted 2 March 2013
Available online 14 March 2013

Abstract

Stress development during cofiring a bi-layer laminate with a non-magnetic $(Cu_{0.2}Zn_{0.8}O)$–$(Fe_2O_3)_{0.8}$ (CZF) and a magnetic $(Ni_{0.25}Cu_{0.25}Zn_{0.5}O)$–$(Fe_2O_3)_{0.75}$ (NCZF) ferrite layer has been investigated by measuring camber development and shrinkage rate difference. Development of camber follows a similar trend to that of linear shrinkage rate difference between CZF and NCZF. The sintering mismatch stress generated during cofiring is much less than those of sintering potentials, resulting in no cofiring defects observed at the interface of CZF/NCZF. Results of electrical and magnetic property measurements show that the multilayer NCZF inductor with an embedded CZF layer has a lower electrical resistance at high frequencies and less significant magnetic inductance reduction with increasing DC current than those of a pure multilayer NCZF inductor.

Keywords: Cofiring; Camber; Stress; Ferrite; Inductor

1. Introduction

Multilayer ferrite inductors with an Ag metallization have been widely used in the electronic industry due to their outstanding magnetic performance and reliability [1,2]. Since the magnetic field, which is generated by an electrical current flowing through Ag conductor, is contained inside of the multilayer ferrite laminate, the inductance decreases significantly when the electrical current exceeds its rated value. This degradation is caused by the generation of magnetic saturation because a closed magnetic field is formed inside of the multilayer ferrite inductor. To solve it, a non-magnetic layer is embedded inside of magnetic ferrite laminate [3–5]. The closed magnetic field formed inside of multilayer magnetic ferrite laminate is thus destroyed and the phenomenon of magnetic saturation disappears. The thus-made multilayer ferrite inductor can withstand a large electrical current, which is one of most desirable characteristics for high voltage conversion application. However, cofiring defects including de-densification, delamination, cracks and camber [6–15] are commonly observed when multilayer laminates with mixed materials are fabricated. These defects are formed mainly due to chemical incompatibility, and densification rate mismatch between different materials [6–12,16,17]. To fabricate defect-free multilayer power ferrite inductors, a non-magnetic ferrite layer with a composition of $(Cu_{0.2}Zn_{0.8}O)$–$(Fe_2O_3)_{0.8}$ (CZF) similar to the magnetic ferrite layer of $(Ni_{0.25}Cu_{0.25}Zn_{0.5}O)$–$(Fe_2O_3)_{0.75}$ (NCZF) is chosen to minimize their chemical and sintering incompatibilities. Both CZF and NCZF can be densified at 900–920 °C. Sintering compatibility between CZF and NCZF is characterized by their linear shrinkage rate difference and camber development of a bi-layer CZF/NCZF laminate. Effects of an embedded CZF layer on the electrical and magnetic properties of multilayer NCZF inductors are also investigated.

2. Experimental procedure

The as-received non-magnetic of $(Cu_{0.2}Zn_{0.8}O)$–$(Fe_2O_3)_{0.8}$ (CZF) and magnetic of $(Ni_{0.25}Cu_{0.25}Zn_{0.5}O)$–$(Fe_2O_3)_{0.75}$ (NCZF) ferrite materials were used. Both of them were prepared by a conventional solid-state reaction and exhibited a pure spinel phase. Both CZF and NCZF had a median

---

[*] Corresponding author. Tel.: +886 3 5742629.
E-mail address: jhjean@mx.nthu.edu.tw (J.-H. Jean).

0272-8842/$ - see front matter © 2013 Elsevier Ltd and Techna Group S.r.l. All rights reserved.
http://dx.doi.org/10.1016/j.ceramint.2013.03.012

particle size of 0.5–1.0 μm (Horiba LA 910, Japan), and could be densified at 900–920 °C for 2 h in air. The densified CZF and NCZF had a thermal expansion coefficient of 8–$10\times10^{-6}\,K^{-1}$ and $9–11\times10^{-6}\,K^{-1}$ at 25–300 °C (TMA, PerkinElmer, USA), and an initial permeability of 1–3 and 180–200 at 1 MHz (E4991A Impedance Analyzer, Agilent, USA), respectively. Green tapes of CZF and NCZF were prepared by tape casting described previously [18]. The green tapes were uniform and had a thickness of about 50 μm. Samples with different thicknesses were prepared by laminating different numbers of green tapes under an iso-static pressure. The lamination condition used in this study was 18 MPa at 80 °C for 5 min. The relative green density of the pressed laminates was measured dimensionally, and the value was in the range of 53±2% of the theoretical density of the fired substrates. The laminates were fired at a heating rate of 2 °C/min from room temperature to 500 °C to remove binder. To remove the organic completely, the laminates were held at 500 °C for 1 h. After binder burnout, the samples were fired at a heating rate of 5 °C/min to 700–1100 °C, and the shrinkage was measured non-isothermally using a thermal mechanical analyzer (TMA, PerkinElmer, USA). For the asymmetric laminates, a bi-layer CZF/NCZF laminate was formed by stacking 5-layer CZF and NCZF green tapes on each side of laminate to enhance curvature development, which was recorded continuously by taking photographs using an optical system [19]. Cambers (curvatures) were determined by measuring the bending curvature of the samples on magnified photographs taken at different temperatures. Multilayer NCZF inductors with Ag metallization were prepared by a conventional green line process and its final dimension was $2.0\times1.2\times0.8$ mm. To investigate the effects of CZF on electrical and magnetic properties of multilayer NCZF inductors, a thin layer of non-magnetic CZF (~50 μm) was embedded in the middle of NCZF laminate, and cofired at 915 °C for 2 h. Electrical resistance (R_{ac}) and magnetic inductance of multilayer ferrite inductors were measured at different frequencies ranging from 10^{-4} to 10 MHz, and at different DC currents, respectively. Microstructure of densified multilayer CZF/NCZF laminates was examined by a scanning electron microscopy (SEM, JEOL, JSM-6500F, Japan), and composition was analyzed by energy-dispersive X-ray spectroscopy (EDX, JOEL, Japan).

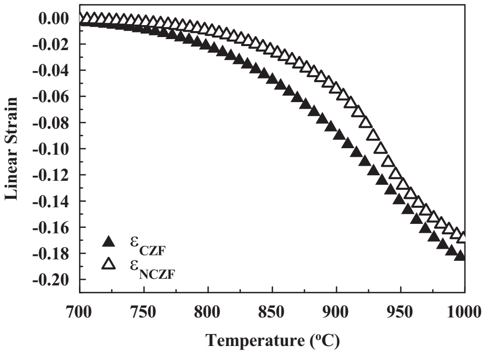

Fig. 1. Linear strain (ε) as a function of temperature for CZF (ε_{CZF}) and NCZF (ε_{NCZF}), measured in the X direction and fired at a heating rate of 5 °C/min.

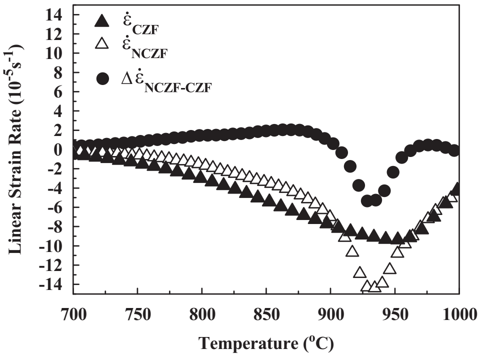

Fig. 2. Linear strain rate as a function of temperature for CZF ($\dot{\varepsilon}_{CZF}$) and NCZF ($\dot{\varepsilon}_{NCZF}$), and linear strain rate difference between NCZF and CZF ($\Delta\dot{\varepsilon}_{NCZF-CZF}$), measured in the X direction of laminate and fired at a heating rate of 5 °C/min.

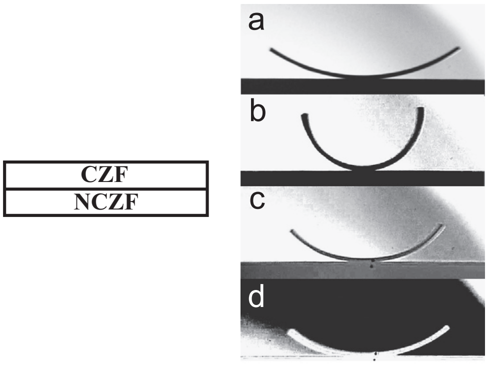

Fig. 3. Photos of camber development at (a) 750, (b) 850, (c) 900, and (d) 1000 °C, fired at a heating rate of 5 °C/min.

3. Results

Results of linear strain (ε) as a function of temperature for CZF and NCZF are shown in Fig. 1. The ε is obtained by $\ln(L(t)/L_o)$ where L_o is the initial length and $L(t)$ is the length of samples at time, t. A similar onset shrinkage temperature of 700–725 °C is observed for both ferrites. Fig. 2 illustrates the linear strain rate curves of CZF and NCZF, which are obtained by taking derivative of the results in Fig. 1. The linear strain rate difference between CZF and NCZF ($\Delta\dot{\varepsilon}_{NCZF-CZF}$) is also presented in Fig. 2, where CZF shrinks more rapidly than NCZF at temperatures below 900 °C, but more slowly above it. No significant difference in the linear strain rates is found above 960 °C.

Fig. 3 shows camber development of bi-layer CZF/NCZF laminates at different temperatures. A positive curvature is defined when the laminate bends toward CZF (top) side. As sintering starts, a positive curvature is promptly observed. This is due to the fact that CZF densifies more rapidly than NCZF (Fig. 2). To eliminate the effect of sample thickness, the curvature data are normalized by the total thickness of laminate

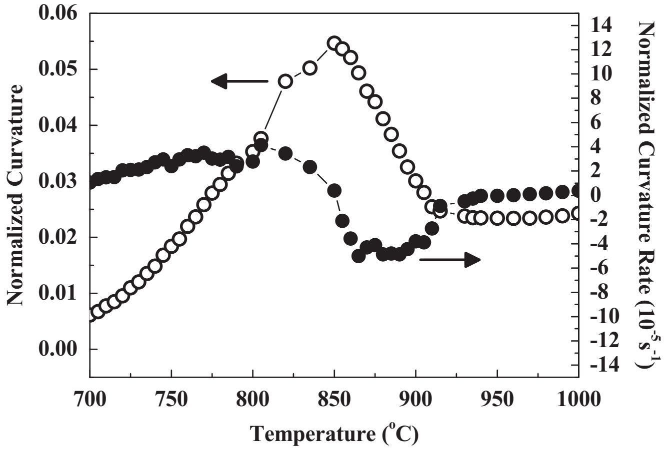

Fig. 4. Normalized curvature of a bi-layer CZF/NCZF laminate and its rate as a function of temperature, fired at a heating rate of 5 °C/min.

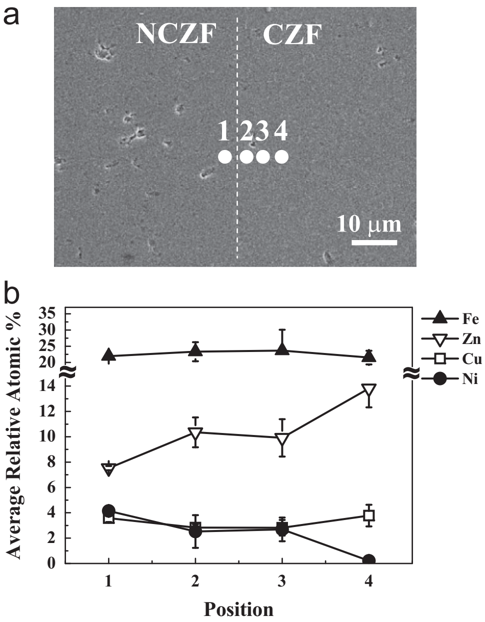

Fig. 5. (a) Microstructural examination and (b) EDX analysis of the interfacial area between CZF and NCZF, fired at a heating rate of 5 °C/min to 1000 °C.

as $\kappa=(h_{\mathrm{CZF}}+h_{\mathrm{NCZF}})/r$ where r is the radius of curvature. Fig. 4 summarizes the results of normalized curvature (κ) and its rate ($\dot{\kappa}$) as a function of temperature. A positive curvature with a maximum at 840–860 °C is found at all temperatures investigated. At temperatures below 840–860 °C, a positive curvature rate is observed. As firing continues, the deformation rate becomes negative with a maximum at 870–890 °C, but reaches insignificant values at temperatures above 925 °C. Comparing with linear shrinkage rate difference in Fig. 2, the results of camber rate in Fig. 4 exhibit a similar trend with a 25–40 °C shift to lower temperatures. Microstructural and compositional examination of the interface between CZF and NCZF are shown in Fig. 5. Both CZF and NCZF are dense, and no cofiring defects are observed at the interface between CZF and NCZF, as shown in Fig. 5(a). As expected that diffusion of Zn from CZF to NCZF, and Ni from NCZF to CZF taking place during cofiring is confirmed by EDX results in Fig. 5(b).

Effects of an embedded CZF layer on the electrical and magnetic properties of multilayer NCZF inductor are illustrated in Figs. 6(a) and (b), respectively. The electrical resistance (R_{ac}) of the multilayer NCZF inductor with an embedded CZF layer is always lower than that without it, and the difference becomes much more significant at high frequencies, as shown in Fig. 6(a). For the magnetic property results in Fig. 6(b), the inductance decreases with increasing DC current for both inductors. The degree of reduction in magnetic inductance ($\Delta I/I_{\mathrm{o}}$) becomes less dramatic for the multilayer NCZF inductor with the embedded CZF layer than that without it. This phenomenon becomes more evident at large DC currents. The above results clearly indicate that the closed magnetic field formed inside of multilayer NCZF inductor is destroyed and the phenomenon of magnetic saturation disappears by the presence of the non-magnetic CZF layer.

4. Discussion

The linear shrinkage rate difference between different materials has been previously identified to be the root cause for the development of stress and camber during cofiring a bi-layer ceramic laminate [10–12]. According to a viscous model analysis, the average biaxial stress in the CZF layer ($\sigma_{CZF}^{AVG\text{-}A}$) generated during cofiring the bi-layer laminate of CZF/NCZF can be calculated by [6,7]

$$\sigma_{CZF}^{AVG\text{-}A}=\left[\frac{m^4+mn}{n^2+2mn(2m^2+3m+2)+m^4}\right]\hat{\sigma}_{CZF} \tag{1}$$

where m and n are the thickness ($m=h_{\mathrm{CZF}}/h_{\mathrm{NCZF}}$) and viscosity ratio (Eq. (2)) between CZF and NCZF, respectively. $\hat{\sigma}_{CZF}$ is the nominal viscous mismatch stress, which can be calculated from linear shrinkage rate difference (Eq. (3)) or camber rate (Eq. (4)). SEM micrographs are used to determine the thickness ratio (m) at different temperatures, which varies in the range of 0.9–1.0. The viscosity ratio (n) is determined by

$$n=\left(\frac{E_p^{CZF}}{1-\upsilon_p^{CZF}}\right)\left(\frac{1-\upsilon_p^{NCZF}}{E_p^{NCZF}}\right) \tag{2}$$

where E_P^{CZF} and E_P^{NCZF} are the porous uniaxial viscosities, and υ_P^{CZF} and υ_P^{NCZF}, the viscous Poisson's ratio of porous CZF and NCZF, respectively. Cyclic loading TMA is used to measure the uniaxial viscosities of CZF (E_P^{CZF}) and NCZF (E_P^{NCZF}) [6,7,11,12], as shown in Fig. 7 where both of them decrease with increasing temperature at 750–920 °C due to microstructural softening, but increase with increasing temperature at 920–1000 °C due to densification. The viscous Poisson's ratio of CZF (υ_P^{CZF}) and NCZF (υ_P^{NCZF}) is related to the relative sintered density (ρ) by $\upsilon_P=1/2\sqrt{\rho/(3-2\rho)}$ [20,21], which ranges from 0.28 for ρ=0.6 to 0.5 for ρ=1.0. The nominal viscous mismatch stress in the CZF layer ($\hat{\sigma}_{CZF}$) in Eq. (1) is calculated using the linear strain rate difference between CZF and NCZF ($\Delta\dot{\varepsilon}_{NCZF-CZF}$) (Fig. 2) and the porous uniaxial

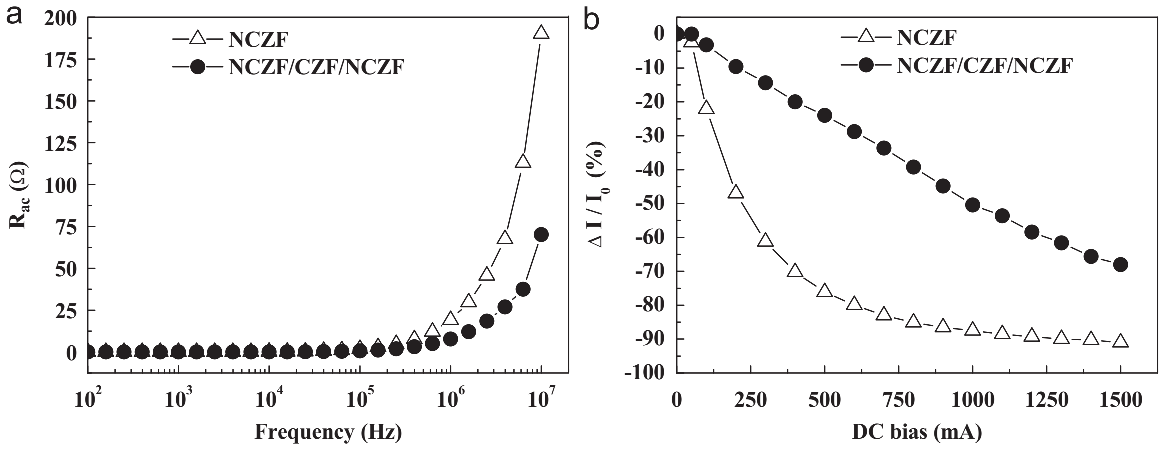

Fig. 6. Effects of an embedded CZF layer on (a) electrical resistance (R_{ac}) as a function of frequency and (b) magnetic inductance reduction ($\Delta I/I_o$) as a function of DC bias of multilayer NCZF inductors.

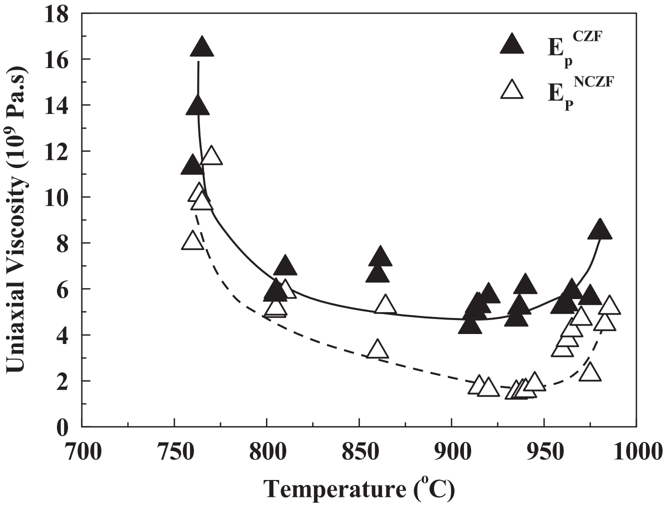

Fig. 7. Uniaxial viscosity (E_P) of CZF and NCZF as a function of temperature, fired at a heating rate of 5 °C/min.

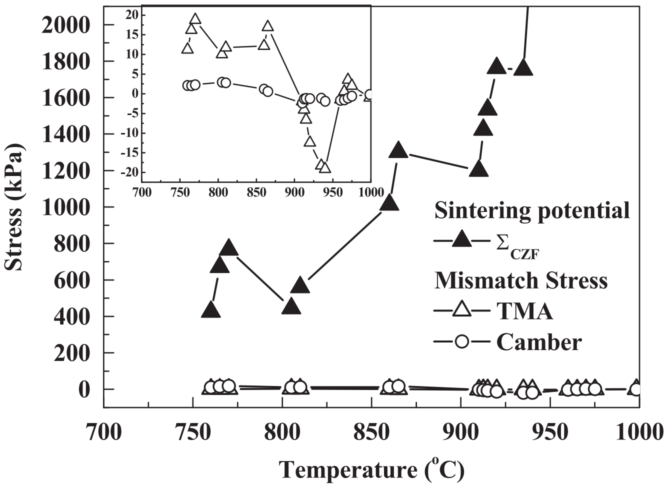

Fig. 8. Sintering potential (Σ_{CZF}) and average sintering mismatch stress ($\sigma_{CZF}^{AVG\text{-}A}$) of CZF in the bi-layer CZF/NCZF laminate as a function of temperature. The average sintering mismatch stresses shown in the inset were calculated by linear strain rate difference from TMA data, and normalized curvature rate data.

viscosities (Fig. 7) by [6,7]

$$\hat{\sigma}_{CZF}=\frac{E_P^{CZF}}{1-\upsilon_P^{CZF}}\Delta\dot{\varepsilon}_{NCZF-CZF} \tag{3}$$

Incorporating the above data of m, n and $\hat{\sigma}_{CZF}$ into Eq. (1), the average sintering mismatch stress in the CZF layer ($\boldsymbol{\sigma}_{CZF}^{AVG\text{-}A}$) is determined and the results are shown in the inset of Fig. 8, where the mismatch stress varies in the range of ±20 kPa at 750–1000 °C.

With the normalized camber rate ($\dot{\kappa}$) data in Fig. 4, the nominal viscous mismatch stress in the CZF layer ($\hat{\sigma}_{CZF}$) can also be calculated by [6,7]

$$\hat{\sigma}_{CZF}=\left[\frac{m^4n^2+2mn(2m^2+3m+2)+1}{6(m+1)^2mn}\right]E_p^{CZF}\dot{\kappa} \tag{4}$$

Again, with the above data of nominal viscous mismatch stress ($\hat{\sigma}_{CZF}$), m and n, the average sintering mismatch stress in the CZF layer ($\sigma_{CZF}^{AVG\text{-}A}$) is calculated by Eq. (1) and the results are shown in the inset of Fig. 8. The mismatch stress varies in the range of ±5 kPa, slightly less than those calculated by linear shrinkage rate difference. The above insignificant difference in the calculated mismatch stresses indicates an excellent sintering compatibility existing between CZF and NCZF layers because the camber rate is measured under cofiring but the linear shrinkage rate difference under free sintering.

Sintering compatibility between CZF and NCZF can be further confirmed by comparing the values of the average sintering mismatch stress in the CZF layer ($\boldsymbol{\sigma}_{CZF}^{AVG\text{-}A}$) with its own sintering potential (Σ_{CZF}), as shown in Fig. 8. Note that the sintering potential is the driving force of free sintering and related to the porous bulk viscosity (K_P^{CZF}) and linear strain rate ($\dot{\varepsilon}_{CZF}$) as $\Sigma_{CZF}=3K_P^{CZF}\dot{\varepsilon}_{CZF}$ assuming an isotropic shrinkage [20,21]. The K_P^{CZF} can be calculated by $K_P^{CZF}=E_P^{CZF}(3(1-2\upsilon_P^{CZF}))^{-1}$ [20,21]. At all temperatures investigated, the sintering potentials of CZF (Σ_{CZF}) varies in the range of 400–2000 kPa, which are much larger than those of sintering mismatch stresses, ±20 kPa. This explains no significant defects (Fig. 5), such as poor densification, delamination and cracks, formed in the multilayer CZF/NCZF laminates during cofiring.

5. Conclusions

A bi-layer laminate consisted of a non-magnetic $(Cu_{0.2}Zn_{0.8}O)–(Fe_2O_3)_{0.8}$ (CZF) and a magnetic $(Ni_{0.25}Cu_{0.25}Zn_{0.5}O)–(Fe_2O_3)_{0.75}$ (NCZF) ferrite layer has been used to investigate stress and camber development during cofiring. No cofiring defects such as poor densification and cracks are observed in the multilayer CZF/NCZF laminate, which is attributed to the sintering mismatch stress generated much smaller than those of sintering potentials. The multilayer NCZF inductor with the embedded CZF layer exhibits a lower electrical resistance at high frequencies and less significant reduction in magnetic inductance with increasing DC current than that without it.

Acknowledgments

Funding for this study has been provided by the National Science Council of the Republic of China under Grant no. 99-2221-E-007-036-MY3.

References

[1] M. Damnjanovic, G. Stojanovic, V. Desnica, L. Zivanov, R. Raghavendra, P. Bellew, N. Mcloughlin, Analysis, design, and characterization of ferrite EMI suppressors, IEEE Transactions on Magnetics 42 (2006) 270–277.

[2] H. Su, H.W. Zhang, X.L. Tang, Y.L. Jing, B.Y. Liu, Electromagnetic properties of Mg-substituted NiCuZn ferrites for multilayer chip inductors applications, IEEE Transactions on Magnetics 45 (2009) 2050–2052.

[3] A. Nakano, S. Saito, T. Nomura, Composite multilayer parts. US Patent 5476728, December 19, 1995.

[4] K. Tsuzuki, Multilayer coils. Eur. Patent 1739695, March 14, 2007.

[5] H.I. Hsiang, L.T. Mei, C.S. Hsi, Y.L. Liu, F.S. Yen, Electrical properties of low-temperature sintered copper and titanium-codoped copper zinc ferrites, Journal of Alloys and Compounds 502 (2010) 163–168.

[6] P.Z. Cai, G.L. Messing, D.L. Green, Constrained densification of alumina/zirconia hybrid laminates, I: experimental observations of processing defects, Journal of the American Ceramic Society 80 (1997) 1929–1939.

[7] P.Z. Cai, G.L. Messing, D.L. Green, Constrained densification of alumina/zirconia hybrid laminates, II: viscous stress computation, Journal of the American Ceramic Society 80 (1997) 1940–1948.

[8] T. Cheng, R. Raj, Flaw generation during constrained sintering of metal–glass multilayer films, Journal of the American Ceramic Society 72 (1989) 1649–1655.

[9] J.H. Jean, C.R. Chang, Cofiring kinetics and mechanisms of an Ag-metallized ceramic-filled glass electronic package, Journal of the American Ceramic Society 80 (1997) 3084–3092.

[10] J.H. Jean, C.R. Chang, Z.C. Chen, Effect of densification mismatch on camber development during cofiring of nickel-based multilayer ceramic capacitors, Journal of the American Ceramic Society 80 (1997) 2401–2406.

[11] R. Zuo, E. Aulbach, J. Rodel, Experimental determination of sintering stresses and sintering viscosities, Acta Metallurgica et Materialia 51 (2003) 4563–4574.

[12] R.T. Hsu, J.H. Jean, Key factors controlling camber behavior during the cofiring of bi-layer ceramic dielectric laminates, Journal of the American Ceramic Society 88 (2005) 2429–2434.

[13] A.G. Evans, J.W. Hutchinson, The thermomechanical integrity of thin films and multilayers, Acta Metallurgica et Materialia 43 (1995) 2507–2530.

[14] C. Hillman, Z. Suo, F.F. Lange, Cracking of laminates subjected to biaxial tensile stresses, Journal of the American Ceramic Society 79 (1996) 2127–2133.

[15] S. Ho, C. Hillman, F.F. Lange, Z. Suo, Surface cracking in layers under biaxial, residual compressive stress, Journal of the American Ceramic Society 79 (1996) 2353–2359.

[16] D. Ravi, D.J. Green, Sintering stresses produced by density differences in bi-layer structures, Journal of the European Ceramic Society 26 (2006) 17–25.

[17] S.E. Schoenberg, D.J. Green, G.L. Messing, Stresses and distortion due to green density gradient during densification, Journal of the American Ceramic Society 89 (2006) 3017–3033.

[18] T.M. Peng, R.T. Hsu, J.H. Jean, Low-fire processing and properties of ferrite + dielectric ceramic composite, Journal of the American Ceramic Society 89 (2006) 2822–2827.

[19] G.Q. Lu, R.C. Sutterlin, T.K. Gupta, Effect of mismatched sintering kinetics on camber in a low-temperature cofired ceramic package, Journal of the American Ceramic Society 76 (1993) 1907–1914.

[20] R.K. Bordia, G.W. Scherer, On constrained sintering – I, constitutive model for a sintering body, Acta Metallurgica 36 (1988) 2393–2397.

[21] R.K. Bordia, G.W. Scherer, On constrained sintering—II, comparison of constitutive models, Acta Metallurgica 36 (1988) 2399–2409.